

Large anomalous Nernst effect at room temperature in a chiral antiferromagnet

Muhammad Ikhlas^{1,*}, Takahiro Tomita^{1,*}, Takashi Koretsune^{2,3}, Michi-To Suzuki², Daisuke Nishio-Hamane¹, Ryotaro Arita^{2,4}, Yoshichika Otani^{1,2,4}, Satoru Nakatsuji^{1,4,*}

¹*Institute for Solid State Physics, University of Tokyo, Kashiwa 277-8581, Japan*

²*RIKEN-CEMS, 2-1 Hirosawa, Wako 351-0198, Japan*

³*PRESTO, Japan Science and Technology Agency (JST), 4-1-8 Honcho Kawaguchi, Saitama 332-0012, Japan.*

⁴*CREST, Japan Science and Technology Agency (JST), 4-1-8 Honcho Kawaguchi, Saitama 332-0012, Japan.*

Temperature gradient in a ferromagnetic conductor may generate a spontaneous transverse voltage drop in the direction perpendicular to both magnetization and heat current. This anomalous Nernst effect (ANE) has been considered to be proportional to the magnetization¹⁻⁷, and thus observed only in ferromagnets, while recent theories indicate that ANE provides a measure of the Berry curvature at the Fermi energy E_F ^{8,9}. Here we report the observation of a large ANE at zero field in the chiral antiferromagnet Mn_3Sn ¹⁰. Despite a very small magnetization $\sim 0.002 \mu_B/Mn$, the transverse Seebeck coefficient at zero field is $\sim 0.35 \mu V/K$ at room temperature and reaches $\sim 0.6 \mu V/K$ at 200 K, comparable with the maximum value known for a ferromagnetic metal. Our first-principles calculation reveals that the large ANE

*These two authors contributed equally.

comes from a significantly enhanced Berry curvature associated with the Weyl points nearby E_F ¹¹. The ANE is geometrically convenient for the thermoelectric power generation, as it enables a lateral configuration of the modules to efficiently cover the heat source⁶. Our observation of the large ANE in an antiferromagnet paves a way to develop a new class of thermoelectric material using topological magnets to fabricate an efficient, densely integrated thermopile.

Current intensive studies on thermally induced electron transport in ferromagnetic (FM) materials have opened various venues for the research on thermoelectricity and its application¹²⁻¹⁵. This trend has also triggered renewed interest in anomalous Nernst effect (ANE) in FM metals^{3-7,15}, which is the spontaneous transverse voltage drop induced by heat current and is known to be proportional to magnetization (Fig. 1a). On the other hand, the recent Berry phase formulation of the transport properties has led to the discovery that a large anomalous Hall effect (AHE) may arise not only in ferromagnets, but in antiferromagnets and spin liquids, in which the magnetization is vanishingly small^{10,16-23}. As the first case in antiferromagnets, Mn_3Sn has been experimentally found to exhibit a large AHE¹⁰. While the AHE is obtained by an integration of the Berry curvature for all the occupied bands, the ANE is determined by the Berry curvature at E_F ^{8,9}. Thus, the observation of a large AHE does not guarantee the observation of a large ANE. Furthermore, the ANE measurement should be highly useful to clarify the Berry curvature spectra near E_F and to verify the possibility of the Weyl metal recently proposed for Mn_3Sn ¹¹.

Mn_3Sn has a hexagonal crystal structure with space group of $P6_3/mmc$ ²⁴. Mn atoms form a breathing type of a kagome lattice in the ab -plane (Fig. 1b), and the Mn triangles constituting

the kagome lattice are stacked on top along the c -axis forming a tube of face sharing octahedra. On cooling below the Néel temperature of 430 K, Mn magnetic moments of $\sim 3\mu_B$ lying in the ab -plane form a coplanar, chiral magnetic structure characterized by $Q = 0$ wave vector, as clarified by the previous neutron diffraction studies^{25,26}. The combination of geometrical frustration and Dzyaloshinskii–Moriya interaction leads to the inverse triangular spin structure with uniform vector chirality (Fig. 1b)^{25–27}. The chiral antiferromagnetic order has orthorhombic symmetry and thus induces a very tiny magnetization $\sim 2 m\mu_B/\text{Mn}$, which is essential to switch the non-collinear antiferromagnetic structure by using magnetic field. On further cooling below ~ 50 K, a cluster glass phase appears as spins cant toward $[0001]$ (c axis)^{26,28,29}. In this study, we used two as-grown single crystals that have a single phase of hexagonal Mn_3Sn ³⁰ (Methods, Supplementary Information), with slightly different compositions, i.e., $\text{Mn}_{3.06}\text{Sn}_{0.94}$ for “Sample 1”, and $\text{Mn}_{3.09}\text{Sn}_{0.91}$ for “Sample 2” (Methods). Hereafter, we focus on the coplanar magnetic phase at $T > 60$ K.

We first provide clear evidence of the large anomalous Hall and Nernst effects observed in Samples 1&2. Figures 2a & 2b show the field dependence of the Hall resistivity $\rho_H(B)$ in $B \parallel [01\bar{1}0]$ for Samples 1 & 2, respectively. Clearly, there is a sharp jump in $\rho_H(B)$ with a small coercivity of < 200 G. In particular for Sample 2, the size of the jump $\Delta\rho_H$ reaches $\sim 9 \mu\Omega\text{cm}$ at 100 K, which would be equivalent to the Hall resistivity due to an ordinary Hall effect under \sim a few 100 T for free conduction electrons with density of order one electron per Mn atom. To make comparison with theory later, here we take the x , y , and z coordinates along $[2\bar{1}\bar{1}0]$, $[01\bar{1}0]$, and $[0001]$, and estimate the Hall conductivity employing the following expression that takes care of the anisotropy of longitudinal resistivity (Fig. S1), namely, $\sigma_{ji} \approx -\rho_{ji}/(\rho_{jj}\rho_{ii})$, where $(i, j) = (x, y), (y, z), (z, x)$ ²² (Supplementary Information). Figures 2c & 2d show $-\sigma_{zx}$

vs. B for Samples 1 & 2, respectively. The zero field value is $\sim 50 \Omega^{-1}\text{cm}^{-1}$ at 300 K for both samples and it becomes particularly enhanced for Sample 2 at low T s and reaches $120 \Omega^{-1}\text{cm}^{-1}$ at 100 K. The sign change in the Hall effect as a function of field should come from the flipping of the tiny uncompensated moment which follows the rotation of the sublattice moments^{10,25,27}.

Our main experimental observation of a large ANE at room temperature is provided in Fig. 3a. The Nernst signal (transverse thermopower) $-S_{zx}$ of Sample 1 shows a clear rectangular hysteresis with an overall change of $\Delta S_{zx} \sim 0.7 \mu\text{V/K}$ as a function of the in-plane field. This is significantly large for an antiferromagnet and comparable to the values reported for ferromagnets, as we will discuss. While the in-plane Nernst signal exhibits hysteresis with almost no anisotropy, the out-of-plane c -axis component is zero within experimental accuracy, indicating no spontaneous effect in this direction. To further characterize the ANE, we compare it with the magnetization M by plotting in Fig. 3a both $-S_{zx}$ and M sharing an x -axis for the in-plane field. In low fields, the hystereses in both data almost overlap on top of each other. On the other hand, in the higher field region than the coercivity of ~ 100 G, the Nernst effect remains nearly constant, while M increases linearly with field as the sub-lattice moments cant toward the external field direction. These indicate negligible contributions from the normal Nernst effect and presumably the conventional ANE. Furthermore, the remnant Nernst signal at zero field is nearly the same as the saturated value in high field, demonstrating that the single-domain crystal has a large spontaneous Nernst signal as the first case for an antiferromagnet. Similar behavior was found in the field cycles made for Sample 2 (Fig. 3b). A systematic change of the Nernst signal was observed with varying T for both Samples 1 & 2, (Figs. 3c & 3d). For Sample 1, the Nernst signal peaks at ~ 200 K, reaching a value of $0.6 \mu\text{V/K}$, comparable with the maximum value known for a FM metal at room

temperature⁷, while Sample 2 shows a smaller value, peaking at 250 K with 0.3 $\mu\text{V/K}$. A distinct mechanism from the FM case should be at work here as the spontaneous M in Mn_3Sn is nearly 1000 times smaller than ordinary ferromagnets.

To further characterize thermoelectric properties, we measured the longitudinal Seebeck coefficient S_{ii} as a function of T and B . No field dependence was seen in S_{ii} for both samples in the T and B range of the measurements (Supplementary Information, Figs. S2a&b). The Seebeck coefficient for Sample 1 positively peaks at ~ 300 K (Fig. 3c, inset), and takes a minimum value with a negative sign around 50 K. This minimum coincides with the steep rise in the specific heat, and thus, this sign change in $S(T)$ may be related to the effect of phonon drag which typically occurs at $\sim \Theta_D/5$, where Θ_D is the Debye T (Supplementary Information, Fig. S3). Much reduced or no low T sign change was seen for Sample 2 (Fig. 3d, inset).

Generally, temperature gradient ∇T in an open circuit condition is known to produce longitudinal and transverse electric field \mathbf{E} , which can be expressed as $\mathbf{J} = \boldsymbol{\sigma} \cdot \mathbf{E} + \boldsymbol{\alpha} \cdot (-\nabla T) = 0$. Here \mathbf{J} , $\boldsymbol{\sigma}$ and $\boldsymbol{\alpha}$ are the current density, electrical conductivity tensor, and thermoelectric conductivity tensor, respectively. This contains the transverse electric field coming from the thermal Hall effect, which should be negligible as it is usually one order of magnitude smaller than other contributions^{3,4,31}. Assuming this, the Nernst signal can be expressed as $S_{ji} = \rho_{jj}(\alpha_{ji} - S_{ii}\sigma_{ji})$, using the Seebeck coefficient $S_{ii}(= S)$ and the Hall conductivity $\sigma_{ji}(= \sigma_H)$. For this analysis, we used the T dependence of the Hall conductivity shown in Fig. 3e. As shown in Figs. 3c&3d, $-\rho\alpha_{ji}$ estimated using this relation is found to be larger than $-S_{ji}$. We further estimated the transverse thermoelectric conductivity $-\alpha_{zx}$ vs. T (Fig. 3f), which shows a systematic increase on cooling

and has the maximum at $T \sim 150(100)$ K for Sample 1(2). At low T 's, Sample 2 has twice smaller values than Sample 1. In ferromagnets, α_{ji} normally shows an increase on cooling, scaling linearly with M , and decreases linearly with T after M saturates^{3,4}. In Mn_3Sn , however, no correlation with M was seen in $-\alpha_{zx}(T)$ (Fig. 3f).

To further demonstrate the qualitative difference between the ANE observed in Mn_3Sn and in ferromagnets, we made a full logarithmic plot of the anomalous Nernst signal vs. the magnetization for various FM metals and Mn_3Sn (Fig. 4, Methods). Here, the absolute values of the Nernst signal were taken in the magnetically ordered states of each material, and were plotted using B and T as implicit parameters. Similarly to AHE¹⁶, the ANE for ferromagnets is known to be proportional to magnetization. Indeed, Figure 4 confirms such an overall trend for a broad range of FM metals that the anomalous Nernst signal becomes larger with increasing magnetization (Methods). The shaded region which covers all the data points indicates that the anomalous Nernst signal is indeed roughly proportional to the magnetization M , i.e. $|S_{ji}| = |Q_s|\mu_0 M$ with the anomalous Nernst coefficient $|Q_s|$ ranging between 0.05 and 1 $\mu\text{V}/\text{KT}$. Following this relation, Mn_3Sn would have produced the Nernst signal of the order of $0.01 \sim 2$ nV/K with the observed magnetization. Strikingly, however, $S_{ji} \sim 0.3\mu\text{V}/\text{K}$ found at room T is more than 100 times larger than what would be expected based on the above scaling relation for ferromagnets.

The significantly large anomalous Nernst and Hall effects in Mn_3Sn do not follow their conventional scaling relation with M , and thus it is natural to assume that both effects arise through the same mechanism distinct from the conventional one for ferromagnets. The inverse triangular spin structure for Mn_3Sn reduces the lattice symmetry from six fold to two fold in the plane and

thus based on the symmetry argument, the Hall effect may appear in the ab -plane³². Indeed, a recent calculation found that Mn_3Sn may have a large anomalous Hall conductivity²¹, which can be estimated by integrating the Berry curvature of the occupied bands over the entire Brillouin zone⁹. More recently, the possibility of a Weyl metal has been proposed, where the bands crossing E_F have several Weyl points, around which the Berry curvature diverges¹¹.

Another intriguing quantity governed by the Berry curvature is the anomalous Nernst effect. While all the occupied bands are relevant for the anomalous Hall conductivity, only the Berry curvature around the Fermi level determines the ANE or, more precisely, the transverse thermoelectric conductivity α_{ji} ^{8,9}. Therefore, α_{ji} is significantly enhanced when the Berry curvature takes a large value at E_F . To see this in the case of Mn_3Sn , we performed a first-principles calculation, confirming the Weyl points nearby E_F ¹¹. The calculated anomalous Hall conductivity $-\sigma_{zx}$ is found as large as seen in experiment. Theoretically, the extra Mn in Sample 1(2) should dope the conduction electron (Supplementary Information) and thus increase E_F by 0.04 (0.05) eV. Since $-\sigma_{zx}$ forms a peak at $E - E_F \sim 0.065$ eV (Fig. S4), a shift in E_F from +0.04 to +0.05 eV leads to a slight increase in $-\sigma_{zx}$, but a substantial decrease in $-\alpha_{zx}$ (Figs. 3e, 3f inset). This behaviour is consistent with the experimental observation, i.e., Mn doping suppresses $-\alpha_{zx}$ by 50 % at low temperatures, while it enhances $-\sigma_{zx}$ only by ~ 10 % (Figs. 3e, 3f). For a simple Weyl Hamiltonian, σ_{ji} takes its maximum and α_{ji} becomes zero when E_F is located exactly at the Weyl node and on the other hand, α_{ji} becomes strongly enhanced when E_F moves slightly away³³. Clearly, the real band structure of Mn_3Sn should be more complicated. Interestingly, however, our theory also finds that $-\sigma_{zx}$ forms a peak at $E - E_F \sim 0.065$ eV, around which Weyl nodes exist¹¹, and $-\alpha_{zx}$ becomes large when E_F is slightly away from the nodes (Fig. S4). Our results thus

indicate that the ANE in Mn_3Sn is particularly enhanced because of the characteristic structure of the Berry curvature with several Weyl points nearby the Fermi level^{11,33}. Our study further highlights the complementary roles of anomalous Hall conductivity σ_{ji} and transverse thermoelectric conductivity α_{ji} in revealing the topological character of band structure.

Finally, from the viewpoint of application for thermoelectric power generation, ANE could be useful as it facilitates the fabrication of a module structurally much simpler than the conventional one using the Seebeck effect⁶. The orthogonal orientation of the voltage output to the thermal heat flow (Fig. 1a) enables a lateral series connection of a single kind of ferromagnet with alternating magnetization direction (Fig. 1a inset). This simplifies a thermopile structure to efficiently cover the surface of a heat source (Fig. 1a inset), in comparison with the conventional thermoelectric module using the Seebeck effect, which consists of a pillar structure of alternating P- and N-type semiconductors. To increase power density, a thermopile should ideally cover the entire surface of a heat source, and therefore, a micro-fabricated thermopile array has to be arranged as densely as possible. However, as long as a ferromagnet is used, their inherent stray fields may perturb magnetization direction of neighboring modules, and limit the integration density.

Our discovery of a new class of material that produces almost no stray fields but exhibits a large ANE is highly important for the application toward thermoelectric power generation, and it should allow us to design a thermopile with a much denser integration of thermoelectric modules to efficiently cover a heat source than the ferromagnetic counterparts. While the observed values in this work would be still far from the size necessary for application, our study indicates that the magnetic Weyl metals such as Mn_3Sn would be particularly useful to obtain a large ANE

by enhancing the Berry curvature at E_F . Further studies to develop the technology for application such as thin film growth and coercivity control of such magnets will be important to build a thermoelectric power generator.

Figure 1 Thermoelectric module using anomalous Nernst effect, and crystal and magnetic structures of Mn_3Sn . **a**, Schematic illustration of a thermoelectric module based on the anomalous Nernst effect. The anomalous Nernst electric field E appears in the direction of the outer product of the magnetization M and heat current $Q \sim -\nabla T$, and thus can be described as $E = Q_s \mu_0 M \times -\nabla T$, where Q_s is the anomalous Nernst coefficient and μ_0 is vacuum permeability. For the case of Mn_3Sn , the configuration of the sublattice moments is schematically presented. Inset: Schematic illustration of a thermopile made of an array of magnetic modules. The in-plane magnetization directions of neighboring thermoelectric modules are alternated so that the Nernst signal with the same sign can be added up in series. The heat flows along the direction perpendicular to the basal plane of the heat source. **b**, An individual ab -plane of Mn_3Sn . Spheres represent Mn (purple) and Sn (gray) atoms. In addition to the unit cell frame, Mn atoms are connected by lines to illustrate that they form a breathing type of kagome lattice (alternating array of small and large triangles). Mn moments (arrow) form an inverse triangular spin structure.

Figure 2 Magnetic field dependence of the anomalous Hall effect in Mn_3Sn . **a & b**, Field dependence of the Hall resistivity $\rho_H = -\rho_{zx}$ of **a**, Sample 1 ($\text{Mn}_{3.06}\text{Sn}_{0.94}$), and **b**, Sample 2 ($\text{Mn}_{3.09}\text{Sn}_{0.91}$), obtained at 100 K, and 300 K. **c & d**, Field dependence of the Hall conductivity $\sigma_H = -\sigma_{zx}$ of **c**, Sample 1 and **d**, Sample 2 obtained at 100 K, and 300 K.

Figure 3 Anomalous Nernst effect in Mn_3Sn . **a**, Anisotropic field dependence of the Nernst signal $-S_{ji}$ of Sample 1. For comparison, the field dependence of the magnetization M (right axis) for $B \parallel x$ is shown. **b**, $-S_{zx}$ vs. B of Samples 1 & 2 measured at various

temperatures. Here, Samples 1 & 2 refer to crystals with $\text{Mn}_{3.06}\text{Sn}_{0.94}$, and $\text{Mn}_{3.09}\text{Sn}_{0.91}$, respectively. **c** & **d**, T dependence of the zero-field remnant Nernst signal S_{ji} (solid symbol) obtained by the field sweep measurements of **c**, Sample 1 and **d**, Sample 2. The thermoelectric contribution estimated using the relation, $\rho_{jj}\alpha_{ji} = S_{ji} - S_{ii}(\rho_{ji}/\rho_{ii})$, is also shown (open symbol). Insets: Seebeck coefficients S_{xx} , S_{yy} vs. T measured under zero field for **c**, Sample 1 and **d**, Sample 2. **e**, Hall conductivity $-\sigma_{zx}$ vs. T estimated using the relation $\sigma_{zx} = -\rho_{zx}/(\rho_{xx}\rho_{zz})$. The sudden drop in $-\sigma_{zx}$ for Sample 2 is due to the magnetic transition at ~ 60 K (see **f**). Inset: $-\sigma_{zx}$ vs. T for $E - E_F = +40$ (blue) and $+50$ (red) meV obtained by the first-principles calculation. **f**, Transverse thermoelectric conductivity $-\alpha_{zx}$ vs. T (left axis), estimated using the relation, $\alpha_{zx} = (S_{zx}/\rho_{zz}) + \sigma_{zx}S_{xx}$ for the field sweep results (solid circle). For comparison, the T dependences of M (right axis) obtained in $B = 1000$ G $\parallel y$ using a field-cooling (FC, solid symbols) and zero-field-cooling (ZFC, open symbols) sequences are shown. The FC and ZFC results bifurcate at ~ 50 (60) K for Sample 1 (2) due to the magnetic transition. Inset: $-\alpha_{zx}$ vs. T for $E - E_F = +40$ (blue) and $+50$ (red) meV obtained by the first-principles calculation. The error-bars are shown if they are larger than the symbol sizes and indicate the measurement errors that come from the uncertainties of their geometrical factors (Methods).

Figure 4 Magnetization dependence of the spontaneous Nernst effect for ferromagnetic metals and Mn_3Sn . Full logarithmic plot of the anomalous Nernst signal $|S_{ji}|$ vs. the magnetization M for a variety of ferromagnetic metals and Mn_3Sn measured at various temperatures and fields (Methods). It shows the general trend for ferromagnets that $|S_{ji}|$ increases with M . The shaded region indicates the linear relation $|S_{ji}| = |Q_s|\mu_0 M$, with

$|Q_s|$ ranging from $\sim 0.05 \mu\text{V}/\text{KT}$ to $\sim 1 \mu\text{V}/\text{KT}$. The Nernst signal data points for Sample 1 ($\text{Mn}_{3.06}\text{Sn}_{0.94}$) obtained at various temperatures for $B \parallel [01\bar{1}0]$ (blue closed circle) and for Sample 2 ($\text{Mn}_{3.09}\text{Sn}_{0.91}$) for $B \parallel [01\bar{1}0]$ (green closed circle) do not follow the relation, and reach almost the same value as the largest among ferromagnetic metals with three orders of magnitude smaller M .

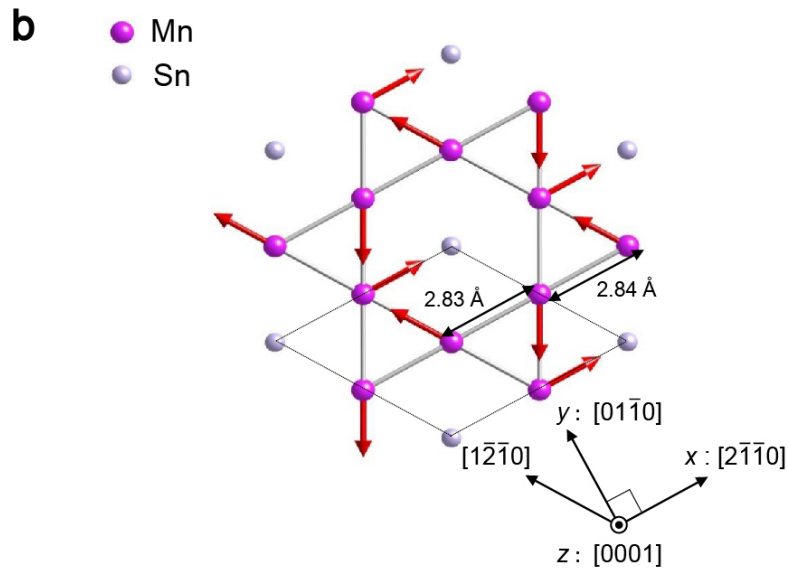
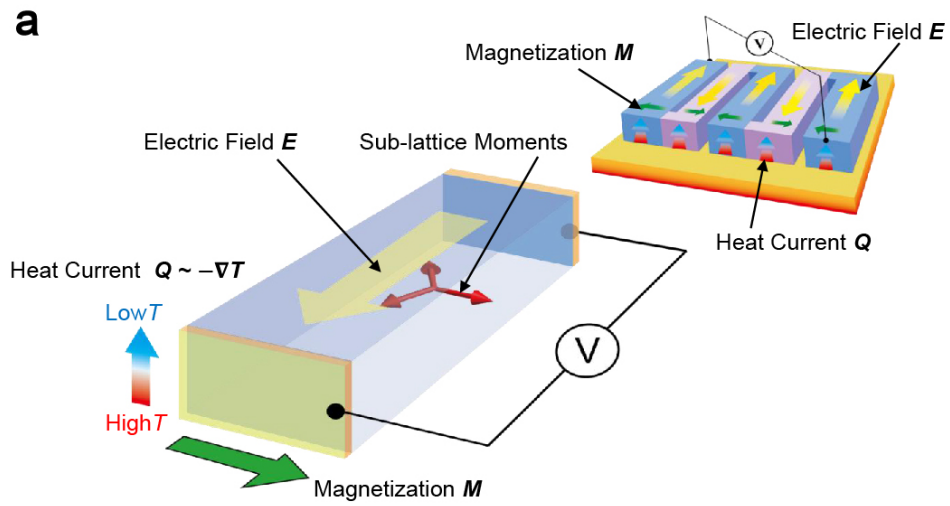


Figure 1

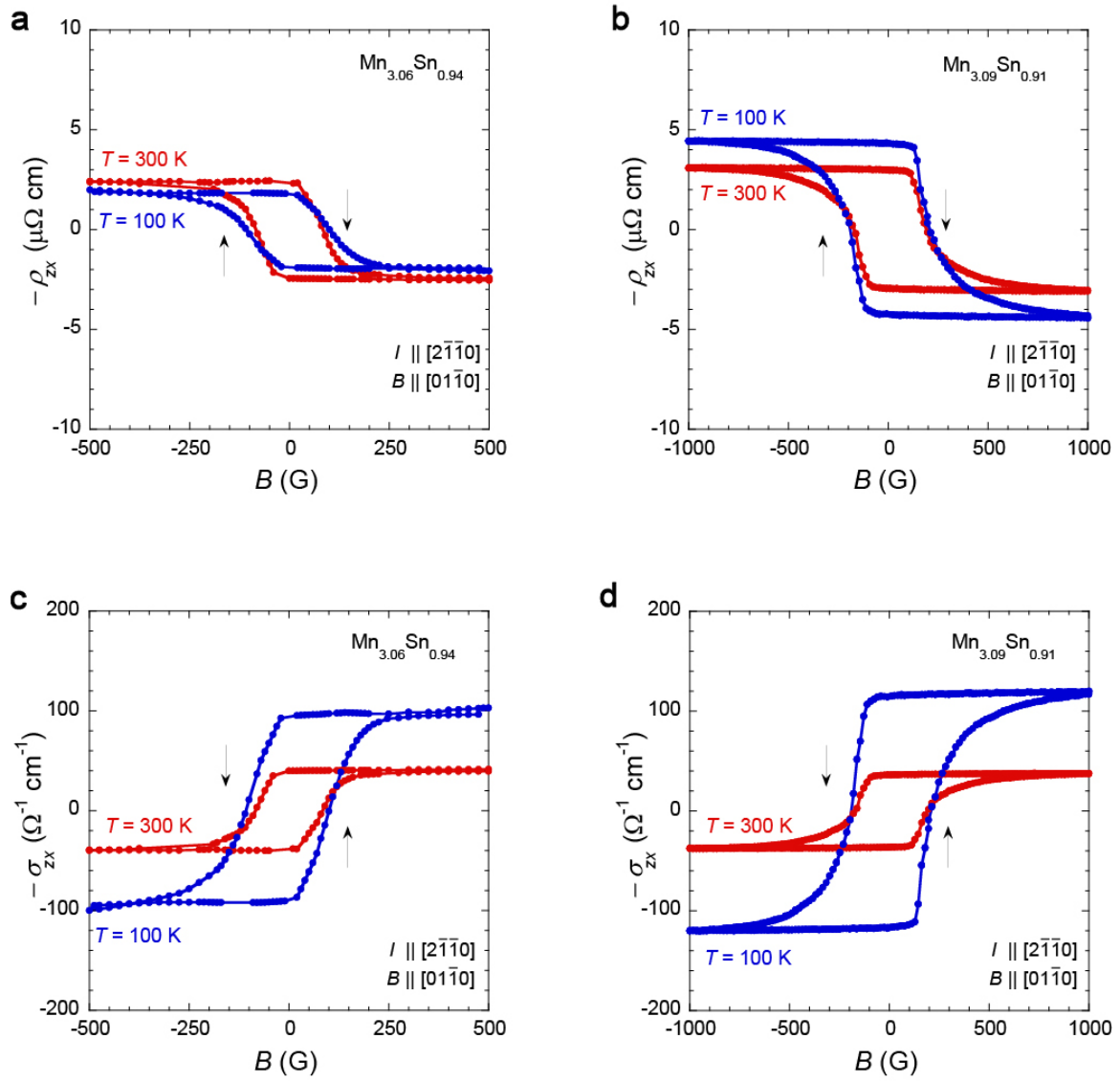


Figure 2

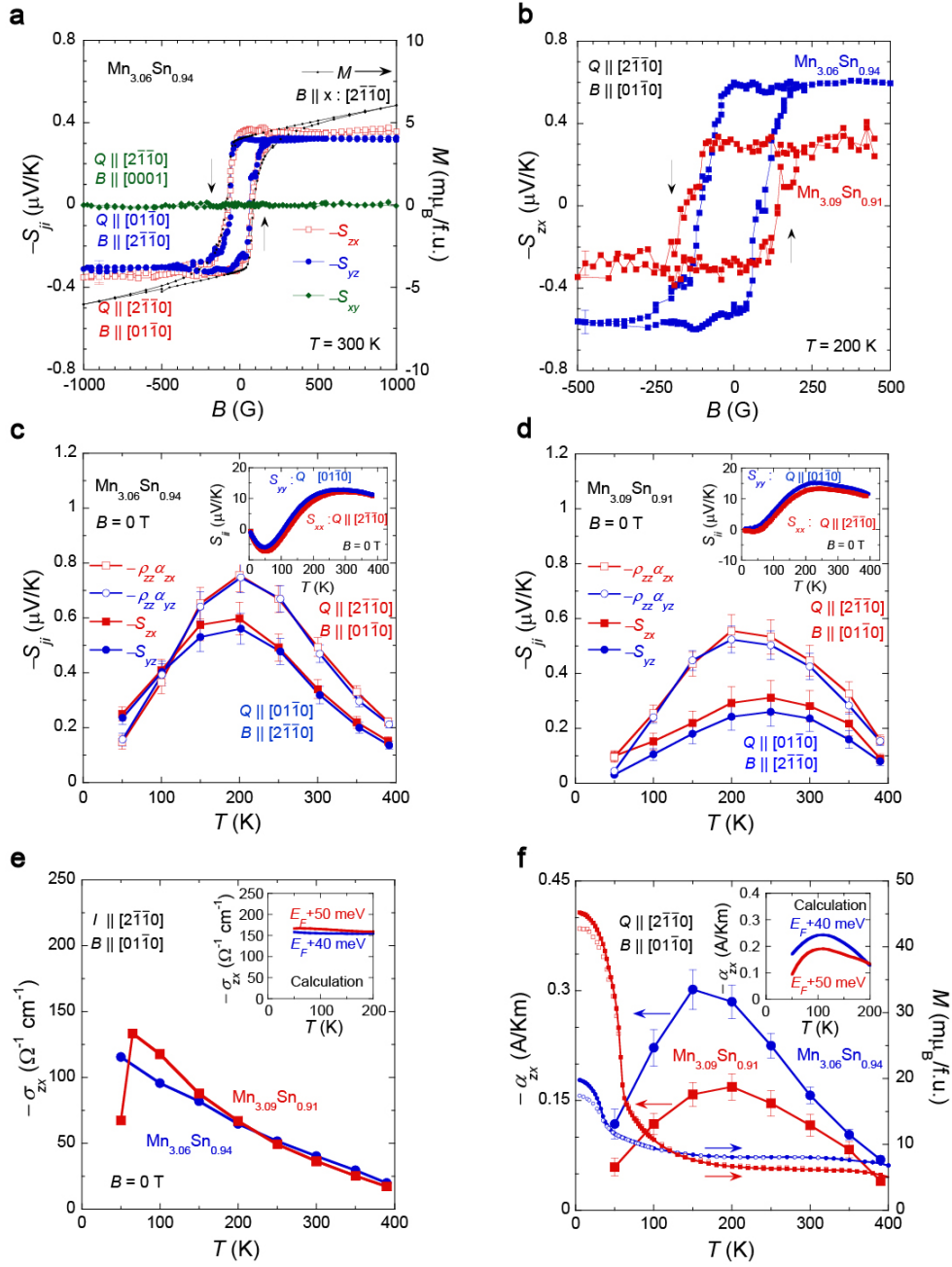


Figure 3

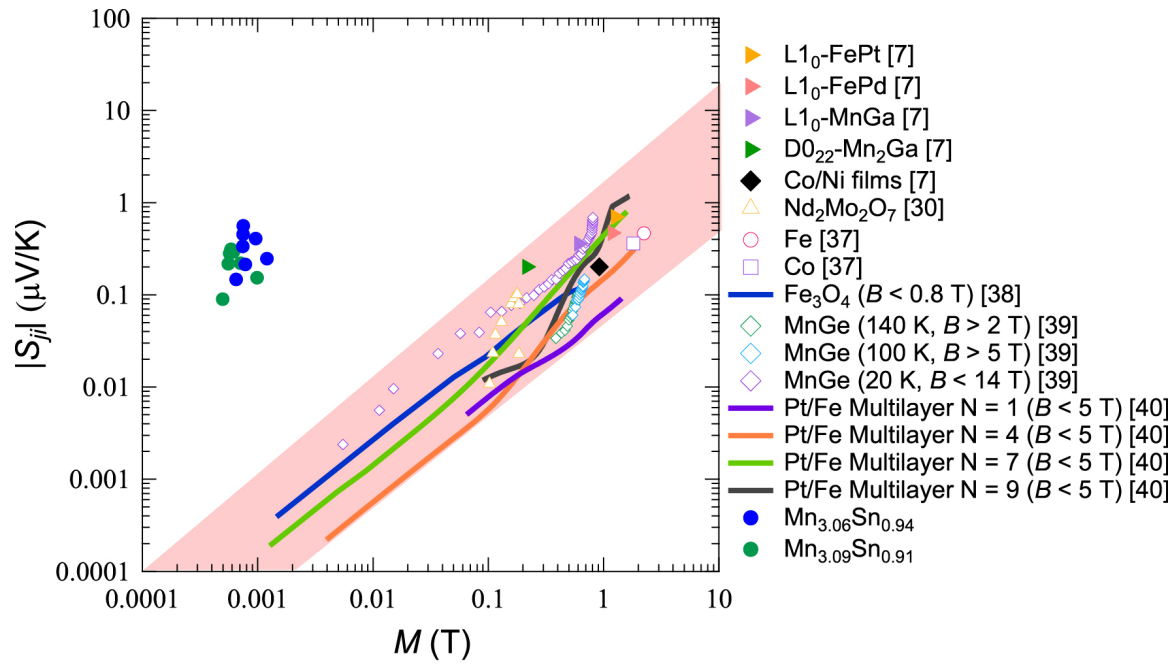


Figure 4

Methods Polycrystalline samples were made by melting the mixtures of manganese and tin in an alumina crucible sealed in an evacuated quartz ampoule in a box furnace at 1050 °C for 6 hours. In preparation for single crystal growth, the obtained polycrystalline materials were crushed into powders, compacted into pellets, and inserted into an alumina crucible which was subsequently sealed in an evacuated silica ampoule. Single crystal growth was performed using a single-zone Bridgman furnace with a maximum temperature of 1080 °C and growth speed of 1.5 mm/h. Analysis using an inductively coupled plasma (ICP) spectroscopy showed that the composition of the single crystal is $\text{Mn}_{3.06}\text{Sn}_{0.94}$ for Sample 1 and $\text{Mn}_{3.09}\text{Sn}_{0.91}$ for Sample 2. Powder X-ray diffraction measurement was performed using diffractometer (RAPID, Rigaku) with a rotating stage in order to remove preferred orientation in the data. One dimensional intensity pattern was extracted from two-dimensional Debye-Scherrer rings which were obtained using transmission mode. Rietveld analysis were performed using RIETAN-FP. All the samples were shown to be single phase, with lattice parameters consistent with previous work (see Supplementary Information and Table S1&S2). After the alignment made using Laue diffractometer, the as-grown single crystals were cut into bar-shaped samples by spark machining for transport and magnetization measurements.

The magnetization measurements were done using a commercial SQUID magnetometer (MPMS, Quantum Design). The associated measurement error is less than a few %. The specific heat measurement was performed using a commercial system (PPMS, Quantum Design) under zero magnetic field (Supplementary Information). Both longitudinal and Hall resistivities were measured by a standard four-probe method using a commercial system (PPMS, Quantum Design). Electrical contacts were made by spot-welding gold wires for the longitudinal and transverse voltage probes, both of which were placed ~ 1.5 mm apart on the sample with a typical current cross

section area of $\sim 0.20 \text{ mm}^2$. In addition, thermoelectric properties were jointly measured by the one-heater and two-thermometer configuration using a commercial system (PPMS, Quantum Design). For thermoelectric measurements, the samples have the typical dimension of $\sim 10 \times 2 \times 2 \text{ mm}^3$ for Sample 1 ($\text{Mn}_{3.06}\text{Sn}_{0.94}$) and $\sim 5 \times 1.5 \times 1.5 \text{ mm}^3$ for Sample 2 ($\text{Mn}_{3.09}\text{Sn}_{0.91}$). The thermal gradient $-\nabla T$ was applied by a heater at one end of the bar-shaped sample toward a thermal bath at the other end, and was measured by monitoring two thermometers linked to the sample by strips of $\sim 0.5 \text{ mm}$ -wide copper-gold plates along the longest direction of the sample. The distance between the two thermometers are approximately $\sim 5 \text{ mm}$ for Sample 1 and $\sim 2.5 \text{ mm}$ for Sample 2. The magnitude of the transverse voltage ΔV was found to be linearly increasing with the increase of applied temperature difference ΔT . Here, ΔT was typically set to be 1.5 % \sim 2.0 % of the sample temperature for both Seebeck and Nernst measurements. By setting the temperature gradient $-\nabla T$ along a bar-shaped single crystal (x -axis), the thermoelectric longitudinal and transverse emf voltages V_i and V_j were measured in an open circuit condition. The Seebeck coefficient S_{ii} and Nernst signal S_{ji} were then estimated as $S_{ii} = E_i/\nabla T$ and $S_{ji} = E_j/\nabla T$, where E_i and E_j are the longitudinal and transverse electric field. The magnetic field dependence of the Hall resistivity and the Nernst signal was obtained after removing the longitudinal component of the respective transport properties, which is found to be approximately constant as a function of the magnetic field (Supplementary Information).

The measurement errors for the longitudinal resistivity ρ_{ii} , Hall resistivity ρ_{ji} , and Nernst signal S_{ji} , are dominated by the uncertainties of their respective geometrical factors. The uncertainty of the longitudinal resistivity and Hall resistivity is 1-2% and smaller than the symbol sizes used in Figures in the main text and Supplementary Information. The uncertainty in the Nernst

signal S_{ji} is $\sim 10\%$ for Sample 1 and $\sim 20\%$ for Sample 2. The corresponding error-bars for the Nernst signal and the transverse thermoelectric conductivity are given in Fig. 3 and Fig. S2.

The transverse thermoelectric conductivity α_{zx} was calculated using the Berry curvature formula⁸ with the first-principles electronic structure. The density functional theory calculation was performed within the generalized-gradient approximation³⁴ as implemented in the quantum-ESPRESSO package³⁵. A $7 \times 7 \times 7$ k -point grid, ultrasoft pseudopotentials³⁶ and plane wave basis sets with cutoff energies of 80 Ry for wave functions and 320 Ry for charge densities were used. For the Berry curvature calculation, a Wannier-interpolated band structure³⁷ with $40 \times 40 \times 40$ k -point grid was employed.

The specimens for transmission electron microscope were prepared by Ar ion milling using a JEOL Ion-Slicer operated at 5.5 kV and 150 μ A under a low beam angle of 2.5° . Selected area electron diffraction and high resolution lattice images were obtained using a transmission electron microscope (JEOL JEM-2010F) operated at 200 kV. High resolution lattice images were simulated by MacTempas software.

Figure 4 was made using the ANE results obtained for various ferromagnets well below their Curie temperatures, as reported in literature including $L1_0$ -FePt (300 K)⁷, $L1_0$ -FePd (300 K)⁷, $L1_0$ -MnGa (300 K)⁷, $D0_{22}$ -Mn₂Ga (300 K)⁷, Co/Ni films (300 K)⁷, $Nd_2Mo_2O_7$ ($T < T_c = 73$ K, $B = 1$ T \parallel [111])³¹, Fe (300 K)³⁸, Co (300 K)³⁸, Fe_3O_4 (300 K, $B < 0.8$ T)³⁹, MnGe (140 K, $B > 2$ T)⁴⁰, MnGe (100 K, $B > 5$ T)⁴⁰, MnGe (20 K, $B < 14$ T)⁴⁰, and Pt/Fe Multilayer $N = 1 \sim 9$ (300 K, $B < 5$ T)⁴¹.

1. Smith, A. W. The Transverse Thermomagnetic Effect in Nickel and Cobalt. *Phys. Rev. (Series I)* **33**, 295–306 (1911).
2. Kondorskii, E. I. & Vasileva, R. Degree of Localization of Magnetic Electron and the Nernst-Ettingshausen Effect in Ferromagnetic Metals. *Sov. Phys. JEPT* **18**, 277–278 (1964).
3. Lee, W.-L., Watauchi, S., Miller, V. L., Cava, R. J. & Ong, N. P. Anomalous Hall Heat Current and Nernst Effect in the $\text{CuCr}_2\text{Se}_{4-x}\text{Br}_x$ Ferromagnet. *Phys. Rev. Lett.* **93**, 226601 (2004).
4. Miyasato, T. *et al.* Crossover Behavior of the Anomalous Hall effect and Anomalous Nernst Effect in Itinerant Ferromagnets. *Phys. Rev. Lett.* **99**, 086602 (2007).
5. Pu, Y., Chiba, D., Matsukura, F., Ohno, H. & Shi, J. Mott Relation for Anomalous Hall and Nernst Effects in $\text{Ga}_{1-x}\text{Mn}_x\text{As}$ Ferromagnetic Semiconductors. *Phys. Rev. Lett.* **101**, 117208 (2008).
6. Sakuraba, Y. *et al.* Anomalous Nernst effect in $\text{L1}_0\text{-FePt/MnGa}$ Thermopiles for New Thermoelectric Applications. *Appl. Phys. Express* **6**, 033003 (2013).
7. Hasegawa, K. *et al.* Material dependence of anomalous Nernst effect in perpendicularly magnetized ordered-alloy thin films. *Appl. Phys. Lett.* **106**, 252405 (2015).
8. Xiao, D., Yao, Y., Fang, Z. & Niu, Q. Berry-phase Effect in Anomalous Thermoelectric Transport. *Phys. Rev. Lett.* **97**, 026603 (2006).
9. Xiao, D., Chang, M.-C. & Niu, Q. Berry phase effects on electronic properties. *Rev. Mod. Phys.* **82**, 1959–2007 (2010).

10. Nakatsuji, S., Kiyohara, N. & Higo, T. Large anomalous Hall effect in a non-collinear antiferromagnet at room temperature. *Nature* **527**, 212–215 (2015).
11. Yang, H. *et al.* Topological Weyl semimetals in the chiral antiferromagnetic materials Mn_3Ge and Mn_3Sn . *New J. Phys.* **19**, 015008 (2017).
12. Bauer, G. E. W., Saitoh, E. & van Wees, B. J. Spin caloritronics. *Nat. Mater.* **11**, 391–399 (2012).
13. Uchida, K. *et al.* Observation of the spin Seebeck effect. *Nature* **455**, 778–781 (2008).
14. Slachter, A., Bakker, F. L., Adam, J.-P. & van Wees, B. J. Thermally driven spin injection from a ferromagnet into a non-magnetic metal. *Nat. Phys.* **6**, 879–882 (2010).
15. Huang, S. Y., Wang, W. G., Lee, S. F., Kwo, J. & Chien, C. L. Intrinsic Spin-Dependent Thermal Transport. *Phys. Rev. Lett.* **107**, 216604 (2011).
16. Nagaosa, N., Sinova, J., Onoda, S., MacDonald, A. H. & Ong, N. P. Anomalous Hall effect. *Rev. Mod. Phys.* **82**, 1539–1592 (2010).
17. Bruno, P. The Berry Phase in Magnetism and the Anomalous Hall Effect. In Kronmüller, H. & Parkins, S. (eds.) *Handbook of Magnetism and Advanced Magnetic Materials*, vol. 1, chap. 22, 540–558 (John Wiley and Sons, Ltd, 2007).
18. Shindou, R. & Nagaosa, N. Orbital ferromagnetism and anomalous Hall effect in antiferromagnets on the distorted fcc lattice. *Phys. Rev. Lett.* **87**, 116801 (2001).

19. Machida, Y., Nakatsuji, S., Onoda, S., Tayama, T. & Sakakibara, T. Time-reversal symmetry breaking and spontaneous Hall effect without magnetic dipole order. *Nature* **463**, 210–213 (2010).
20. Chen, H., Niu, Q. & MacDonald, A. H. Anomalous Hall Effect Arising from Noncollinear Antiferromagnetism. *Phys. Rev. Lett.* **112**, 017205 (2014).
21. Kübler, J. & Felser, C. Non-collinear antiferromagnets and the anomalous Hall effect. *EPL* **108**, 67001 (2014).
22. Kiyohara, N., Tomita, T. & Nakatsuji, S. Giant anomalous hall effect in the chiral antiferromagnet Mn_3Ge . *Phys. Rev. Applied* **5**, 064009 (2016). URL <https://link.aps.org/doi/10.1103/PhysRevApplied.5.064009>.
23. Nayak, A. K. *et al.* Large anomalous Hall effect driven by a nonvanishing Berry curvature in the noncolinear antiferromagnet Mn_3Ge . *Sci. Adv.* **2**, e1501870 (2016).
24. Krén, E., Paitz, J., Zimmer, G. & Zsoldos, É. Study of the magnetic phase transformation in the Mn_3Sn phase. *Physica B* **80**, 226–230 (1975).
25. Tomiyoshi, S. & Yamaguchi, Y. Magnetic structure and weak ferromagnetism of Mn_3Sn studied by polarized neutron diffraction. *J. Phys. Soc. Jpn.* **51**, 2478–2486 (1982).
26. Brown, P. J., Nunez, V., Tasset, F., Forsyth, J. B. & Radhakrishna, P. Determination of the magnetic structure of Mn_3Sn using generalized neutron polarization analysis. *J. Phys. Condens. Matter.* **2**, 9409–9422 (1990).

27. Nagamiya, T., S. & Yamaguchi, Y. Triangular spin configuration and weak ferromagnetism of Mn_3Sn and Mn_3Ge . *Solid State Commun.* **42**, 385–388 (1982).
28. Tomiyoshi, S., Abe, S., Yamaguchi, Y., Yamauchi, H. & Yamamoto, H. Triangular spin structure and weak ferromagnetism of Mn_3Sn at low temperature. *J. Magn. Magn. Mater.* **54–57**, Part 2, 1001–1002 (1986).
29. Feng, W. J. *et al.* Glassy ferromagnetism in Ni_3Sn -type $\text{Mn}_{3.1}\text{Sn}_{0.9}$. *Phys. Rev. B* **73**, 205105 (2006).
30. Ohmori, H., Tomiyoshi, S., Yamauchi, H. & Yamamoto, H. Spin structure and weak ferromagnetism of Mn_3Sn . *J. Magn. Magn. Mater.* **70**, 249–251 (1987).
31. Hanasaki, N. *et al.* Anomalous Nernst Effects in Pyrochlore Molybdates with Spin Chirality. *Phys. Rev. Lett.* **100**, 106601 (2008).
32. Suzuki, M.-T., Koretsune, T., Ochi, M. & Arita, R. Cluster multipole theory for anomalous Hall effect in antiferromagnets. *Phys. Rev. B* **95**, 094406 (2017).
33. Sharma, G., Goswami, P. & Tewari, S. Nernst and magnetothermal conductivity in a lattice model of Weyl fermions. *Phys. Rev. B* **93**, 035116 (2016).
34. Perdew, J., Burke, K. & Ernzerhof, M. Generalized gradient approximation made simple. *Phys. Rev. Lett* **77**, 3865 (1996).
35. Giannozzi, P. *et al.* Quantum espresso: a modular and open-source software project for quantum simulations of materials. *J. Phys: Condens. Matter* **21**, 395502 (2009).

36. Vanderbilt, D. Soft self-consistent pseudopotentials in a generalized eigenvalue formalism. *Phys. Rev. B* **41**, 7892 (1990).
37. Mostofi, A. A. *et al.* wannier90: A tool for obtaining maximally-localised Wannier functions. *Comput Phys. Comm.* **178**, 685–699 (2008).
38. Weischenberg, J., Freimuth, F., Blügel, S. & Mokrousov, Y. Scattering-independent anomalous Nernst effect in ferromagnets. *Phys. Rev. B* **87**, 060406 (2013).
39. Ramos, R. *et al.* Anomalous Nernst effect of Fe₃O₄ single crystal. *Phys. Rev. B* **90**, 054422 (2014).
40. Shiomi, Y., Kanazawa, N., Shibata, K., Onose, Y. & Tokura, Y. Topological Nernst effect in a three-dimensional skyrmion-lattice phase. *Phys. Rev. B* **88**, 064409 (2013).
41. Uchida, K. *et al.* Enhancement of anomalous Nernst effects in metallic multilayers free from proximity-induced magnetism. *Phys. Rev. B* **92**, 094414 (2015).
42. Ziman, J. M. *Electrons and phonons: the theory of transport phenomena in solids* (Oxford University Press, 1960).
43. Izumi, F. & Momma, K. Three-dimensional visualization in powder diffraction. In *Solid State Phenomena*, vol. 130, 15–20 (Trans Tech Publ, 2007).
44. Tomiyoshi, S. Polarized neutron diffraction study of the spin structure of Mn₃Sn. *J. Phys. Soc. Jpn.* **51**, 803–810 (1982).
45. Duan, T. *et al.* Magnetic anisotropy of single-crystalline Mn₃Sn in triangular and helix-phase states. *App. Phys Lett* **107**, 082403 (2015).

46. Cable, J. W., Wakabayashi, N. & Radhakrishna, P. Magnetic excitations in the triangular antiferromagnets Mn_3Sn and Mn_3Ge . *Phys. Rev. B* **48**, 6159–6166 (1993).
47. Tomiyoshi, S., Abe, S., Yamaguchi, Y., Yamauchi, H. & Yamamoto, H. Triangular spin structure and weak ferromagnetism of Mn_3Sn at low temperature. *J. Magn. Magn. Mater.* **54**, 1001–1002 (1986).

Acknowledgements We thank Agung Nugroho, Akito Sakai, Tomoya Higo, Naoki Kiyohara for useful discussions. This work is partially supported by CREST and PRESTO, Japan Science and Technology Agency, and Grants-in-Aid for Scientific Research (16H02209), and Program for Advancing Strategic International Networks to Accelerate the Circulation of Talented Researchers (No. R2604) from the Japanese Society for the Promotion of Science, and by Grants-in-Aids for Scientific Research on Innovative Areas (15H05882, 15H05883, 26103002) of the Ministry of Education, Culture, Sports, Science, and Technology of Japan. The use of the facilities of the Materials Design and Characterization Laboratory at the Institute for Solid State Physics, The University of Tokyo, is gratefully acknowledged.

Author Contributions S.N. and Y.O. conceived the project. S.N. planned the experiments, and T.T., M.I., S.N. performed experiments and analyzed data. T.K., M.S., R.A. performed the first-principles calculations. D.N performed the TEM measurements and analyses. S.N., R.A. wrote the main text. M.I., S.N., T.T., D.N, T.K., M.S., R.A. prepared the supplementary information and figures; All authors discussed the results and commented on the manuscript.

Competing Interests The authors declare that they have no competing financial interests.

Correspondence Correspondence and requests for materials should be addressed to S.N. (email: satoru@issp.u-tokyo.ac.jp).

Data Availability Statement The data that support the plots within this paper and other findings of this study are available from the corresponding author upon reasonable request

Supplementary Information:

Observation of large anomalous Nernst effect at room temperature in a chiral antiferromagnet

Muhammad Ikhlas^{1*}, Takahiro Tomita^{1*}, Takashi Koretsune^{2,3}, Michi-To Suzuki², Daisuke Nishio-Hamane¹, Ryotaro Arita^{2,4}, Yoshichika Otani^{1,2,4}, Satoru Nakatsuji^{1,4}

¹*Institute for Solid State Physics, University of Tokyo, Kashiwa 277-8581, Japan*

²*RIKEN-CEMS, 2-1 Hirosawa, Wako 351-0198, Japan*

³*PRESTO, Japan Science and Technology Agency (JST), 4-1-8 Honcho Kawaguchi, Saitama 332-0012, Japan.*

⁴*CREST, Japan Science and Technology Agency (JST), 4-1-8 Honcho Kawaguchi, Saitama 332-0012, Japan.*

1 Expression of the Hall conductivity σ_{ji} and transverse thermoelectric conductivity α_{ji}

To compare the experimental results with first-principle calculation, we used the following expression for the Hall conductivity σ_{ji} and transverse thermoelectric conductivity α_{ji} , which take into account the anisotropy of the longitudinal resistivity ρ_{ii} ,

$$\sigma_{ji} \approx -\frac{\rho_{ji}}{\rho_{ii}\rho_{jj}}, \quad (1)$$

$$\alpha_{ji} \approx \frac{1}{\rho_{jj}} \left(S_{ji} - \frac{\rho_{ji}}{\rho_{ii}} S_{ii} \right) \quad (2)$$

*These two authors contributed equally.

Here, $(i, j) = (x, y)$, (y, z) , and (z, x) , where x , y , and z are taken to be the coordinates along $[2\bar{1}\bar{1}0]$, $[01\bar{1}0]$, and $[0001]$, respectively ²². In our transport measurements, the applied current I (heat current $Q = -\nabla T$) is defined to be parallel to the i -axis. The longitudinal resistivity ρ_{ii} (Seebeck coefficient S_{ii}) is then measured using contacts placed along the i -axis while the Hall resistivity ρ_{ji} (Nernst signal S_{ji}) is measured using contacts located along the j -axis. Using this definition, the sign of the Hall and the Nernst effect is determined by the right-hand rule.

2 Temperature dependence of the longitudinal resistivity

The temperature dependence of the longitudinal resistivity for Sample 1 ($\text{Mn}_{3.06}\text{Sn}_{0.94}$) and Sample 2 ($\text{Mn}_{3.09}\text{Sn}_{0.91}$) single crystals used is given in Figure S1. Both Samples 1&2 show similar behaviour, i.e the in-plane resistivity is almost isotropic, while the out-of-plane resistivity shows a much stronger temperature dependence than the in-plane resistivity. The residual resistivity ratio ($\text{RRR} = \rho(390 \text{ K}) / \rho(4.2 \text{ K})$) which is a rough measure of the quality of the single crystals shows the value of $\text{RRR} \sim 1.5 - 2.3$ for Sample 1 and $\text{RRR} \sim 1.2 - 1.35$ for Sample 2 in the in-plane direction, and ~ 3.5 for Sample 1 and ~ 2.8 for Sample 2 in the out-of-plane direction. This is consistent with the smaller coercivity observed in the Sample 1 crystals compared to Sample 2, as the coercivity in magnets generally increases with the number of defects and impurities, which may pin a magnetic domain wall. All the components of the longitudinal resistivity have continuous temperature change and nearly saturate above room temperature.

3 Magnetic field dependence of the Seebeck coefficient and the Nernst effect

The magnetic field dependence of the Seebeck coefficient S_{ii} ($i = x, y$) was measured at various temperatures under $B < 0.1$ T along in-plane directions. We found no field dependence within experimental accuracy over all the temperature range between 50 K and 390 K. Figures S2a and S2b represent typical S_{xx} vs. B results obtained at 100 K and 300 K for Samples 1&2, respectively.

The magnetic field dependences of the Nernst effect S_{zx} under $B < 0.1$ T along in-plane directions for Samples 1&2 are shown in Figures S2c and S2d, respectively.

4 Temperature dependence of the Seebeck effect

As shown in Figure 3c inset in the main text, $S_{ii}(T)$ ($i = x, y$) of Sample 1 ($\text{Mn}_{3.06}\text{Sn}_{0.94}$) changes its sign below around 100 K and peaks with a negative amplitude at ~ 50 K. On the other hand, Figure 3d inset shows that a much weaker or nearly no sign change occurs for Sample 2 ($\text{Mn}_{3.09}\text{Sn}_{0.91}$).

The Seebeck coefficient S generally has two contributions: $S = S_d + S_g$. S_d is the contribution from the charge carrier diffusion and S_g is the contribution from the phonon drag effect due to additional charge carriers dragged by the phonon flow. The effect of the phonon drag typically causes a peak in the Seebeck coefficient at $\sim \Theta_D/5$, where Θ_D is the Debye temperature⁴². We made a linear fit to the temperature dependence of the specific heat divided by temperature (Supplementary Figure S3) at the lowest temperature region (2 –4.5 K) using the Einstein-Debye equation, $C/T = \gamma + \beta T^2$, where γ and β are the parameters for the electronic and lattice contributions to the specific heat, respectively. The fit gives $\beta = 0.300 \pm 0.015$ mJ mol⁻¹ K⁻⁴ corresponding to the Debye temperature of $\Theta_D = 280 \pm 14$ K. As shown in Figure 3c inset of the main text, the

minimum of the Seebeck coefficient is roughly located around $\Theta_D/5 = 56$ K, suggesting that the low temperature behaviour may be related to the phonon drag effect. The nearly no sign change in Sample 2 may be related to a larger amount of defects caused by doping, which reduces the phonon lifetime. However, further discussion on the temperature dependence of the Seebeck effect is beyond the scope of this paper, since the multiband nature of this system¹¹ would necessitate more involved analysis. On the other hand, the observed Nernst effect is dominated by the anomalous (spontaneous) contribution and thus transverse thermoelectric conductivity α_{ji} mainly comes from the Berry curvature. Therefore, the contribution from phonon drag in α_{ji} is negligible.

5 Crystal structure of Mn₃Sn

RAPID (Rigaku) X-ray diffractometer (MoK α , $\lambda = 0.7103$ Å) was used at room temperature to investigate the crystal structure of Mn₃Sn. Two-dimensional Debye-Scherrer rings were obtained by the X-ray intensity transmitted through the sample, which were then converted to one-dimensional intensity patterns. The diffraction patterns were analyzed using the Rietveld analysis program RIETAN-FP to determine the precise crystal structure⁴³. We assign a hexagonal structure ($P6_3/mmc$) with the lattice parameters $a = 5.662$ Å and $c = 4.529$ Å⁴⁴. Figure S5 shows the typical result of the X-ray powder pattern obtained for Sample 1 (Mn_{3.06}Sn_{0.94}). The atomic coordinates for the crystal parameter are shown in Table S1 for Sample 1 (Mn_{3.06}Sn_{0.94}) and Table S2 for Sample 2 (Mn_{3.09}Sn_{0.91}). Our results indicate that the samples used in our study have the same crystal structure as those used for previous neutron diffraction measurements^{26,44}.

6 High-resolution transmission electron microscope (TEM) image of Mn_3Sn

Figures S6a and S6b show the high resolution TEM image of Mn_3Sn (using Sample 1 as a representative) taken at room temperature for the (0001) and $(2\bar{1}\bar{1}0)$ planes, respectively. Within the resolution permitted by the maximum operating voltage (200 kV) of the transmission electron microscope (JEOL JEM-2010F), the lattice parameters a and c obtained from the image are in good agreement with the results of our Rietveld analyses discussed above. The overlaid simulation images show the expected position of the Mn and Sn atoms within the lattice.

7 Heat treatment effect on the temperature dependence of the magnetization

A recent paper reported the magnetization curves for Mn_3Sn at different temperatures and found that the in-plane coercive field disappears along with the spontaneous magnetization as the sample is cooled down below 270 K⁴⁵. In contrast to the temperature dependence of the magnetization of our crystal, an additional transition is observed below 270 K in both their magnetization and heat capacity data. They associated this with a transition from the triangular spin structure to a long-period helical spin configuration, which has been observed in earlier neutron scattering studies⁴⁶. It has been known that this transition is observed most pronouncedly in single crystals that were annealed at temperatures below 800°C². Their single crystals were synthesized by slow-cooling the melt from 1000°C to 600°C, and thus a part of this slow-cooling process may play a role of the annealing procedure mentioned above. The mechanism behind this transition is still unknown. On the other hand, the single crystal used in our present paper was prepared from the Bridgman furnace without any additional annealing process, and thus exhibit no transition above 50 K⁴⁷.

8 Relation between the anomalous Nernst effect and the anomalous Hall conductivity

Both the intrinsic anomalous Hall conductivity σ_{zx} and the intrinsic anomalous transverse thermoelectric conductivity α_{zx} are governed by the Berry curvature, $\Omega_n(\mathbf{k})$, as⁸

$$\sigma_{zx} = -\frac{e^2}{\hbar} \int \frac{d\mathbf{k}}{(2\pi)^3} \Omega_{n,y}(\mathbf{k}) f_{n\mathbf{k}}, \quad (3)$$

$$\alpha_{zx} = -\frac{e}{T\hbar} \int \frac{d\mathbf{k}}{(2\pi)^3} \Omega_{n,y}(\mathbf{k}) \left\{ (\varepsilon_{n\mathbf{k}} - \mu) f_{n\mathbf{k}} + k_B T \ln [1 + e^{-\beta(\varepsilon_{n\mathbf{k}} - \mu)}] \right\}. \quad (4)$$

Here, $\varepsilon_{n\mathbf{k}}$, $f_{n\mathbf{k}}$ are the band energy and the Fermi-Dirac distribution function with the band index n and the wave vector \mathbf{k} . Since $\left\{ (\varepsilon_{n\mathbf{k}} - \mu) f_{n\mathbf{k}} + k_B T \ln [1 + e^{-\beta(\varepsilon_{n\mathbf{k}} - \mu)}] \right\}$ is finite only around the Fermi energy, α_{zx} is determined by the Berry curvature around the Fermi energy whereas σ_{zx} is the summation of all the Berry curvature below the Fermi energy. According to these equations, α_{zx} and σ_{zx} are related as follows:

$$\alpha_{zx} = -\frac{1}{e} \int d\varepsilon \frac{\partial f}{\partial \mu} \sigma_{zx}(\varepsilon) \frac{\varepsilon - \mu}{T}. \quad (5)$$

Thus, the size and the sign of α_{zx} are determined by the slope of $\sigma_{zx}(\varepsilon)$ as well as the Berry curvature around the Fermi energy. Indeed, at low temperatures, Eq.(5) can be approximated as

$$\alpha_{zx} = \frac{\pi^2 k_B^2 T}{3|e|} \frac{\partial \sigma_{zx}(\varepsilon)}{\partial \varepsilon} + O(T^3). \quad (6)$$

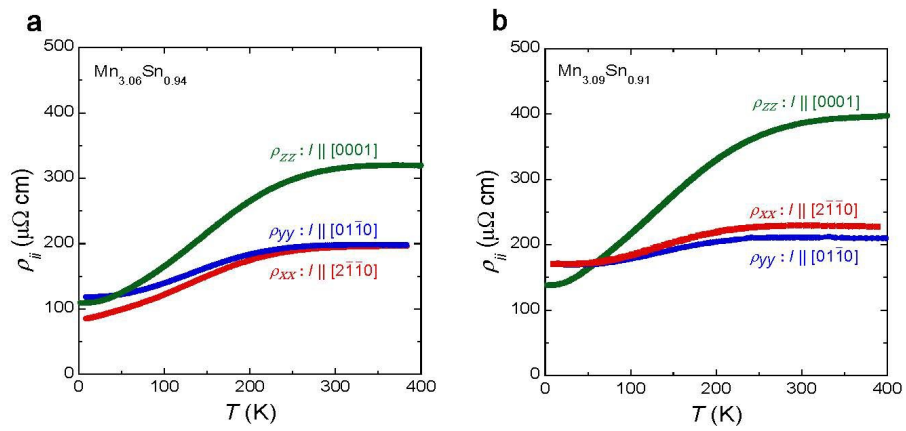
Supplementary Figure S4 indicates the calculated result of the energy dependence of the anomalous Hall and transverse thermoelectric conductivity. According to the result, a slight shift of the Fermi energy leads to a change in the anomalous Hall conductivity. For example, at $\varepsilon = 0.04$ eV, $-\partial \sigma_{zx} / \partial \varepsilon \sim 1000$ (Ωcm)⁻¹(eV)⁻¹. This means that $-\alpha_{zx} \sim 0.0024T$ (A/Km) at low temperature limit, which is consistent with the value of $-\alpha_{zx} = 0.25$ (A/Km) at $T = 100$ K in the inset of Fig. 3f.

In our first-principles calculation for Mn_3Sn , the number of the Mn-s, Mn-d, Sn-s, Sn-p electrons are estimated to be 0.84, 5.85, 1.67, and 3.26, respectively. For $\text{Mn}_{3.06}\text{Sn}_{0.94}$, we can assume that the electron occupancy of the Sn-s, Sn-p and Mn-s orbital are the same as those of Mn_3Sn , since the low-energy states around the Fermi level are mainly formed by the Mn-d orbital. Then the number of electrons doped into the Mn-d orbital is estimated to be 0.024, which shifts the Fermi energy by 0.04 eV for $\text{Mn}_{3.06}\text{Sn}_{0.94}$. With a similar calculation, the shift of the Fermi energy is estimated to be 0.05 eV for $\text{Mn}_{3.09}\text{Sn}_{0.91}$.

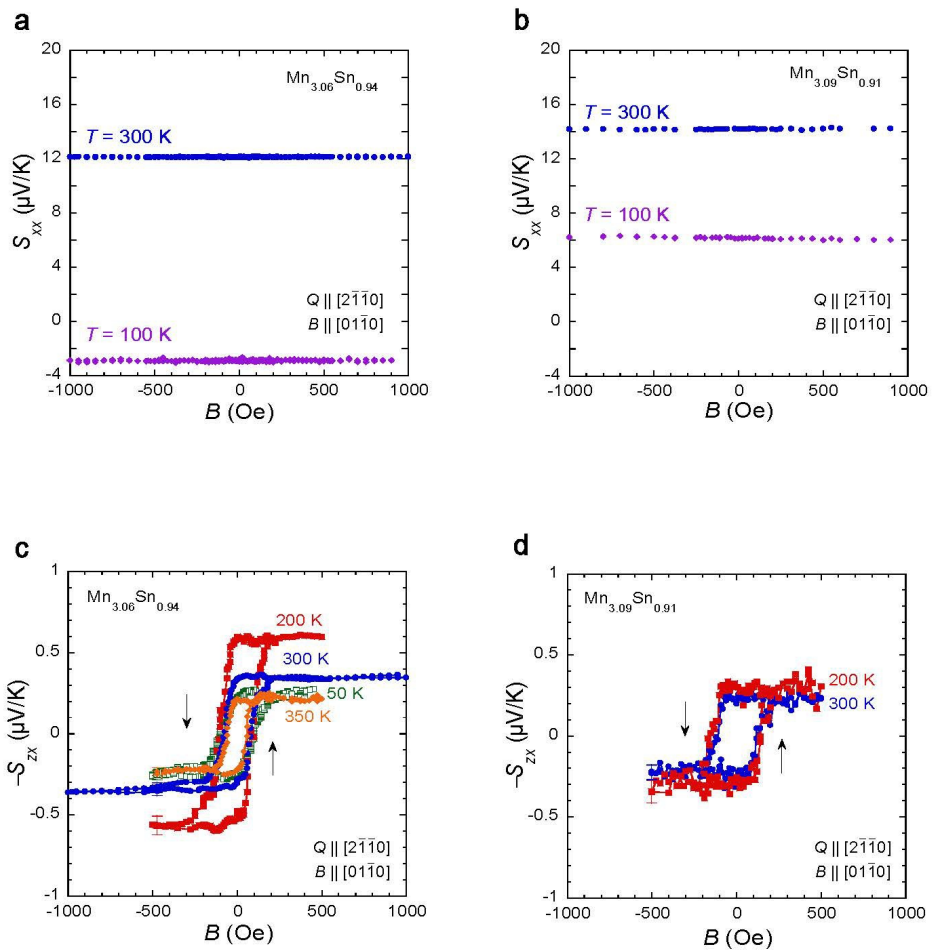
In experiment, a small change in the composition in the crystals used in the present study, namely $\text{Mn}_{3.06}\text{Sn}_{0.94}$ and $\text{Mn}_{3.09}\text{Sn}_{0.91}$, may cause such a shift in E_F . Although the Hall conductivity between the two crystals are almost the same at high temperatures, the difference between the Hall conductivity of the two crystals becomes apparent at low temperatures, as shown in Fig. 3e in the main text. At 100 K, Sample 2 ($\text{Mn}_{3.09}\text{Sn}_{0.91}$) shows larger anomalous Hall conductivity (lower anomalous transverse thermoelectric conductivity) than Sample 1 ($\text{Mn}_{3.06}\text{Sn}_{0.94}$), which semi-quantitatively agrees with first principle-calculation shown in Figure S4. Further investigation is necessary to make a more thorough, quantitative comparison between experiment and theory using samples with a variety of doping levels, and this defines a subject of future study.

The DFT calculation does not take account of the temperature dependence of the local magnetic moment size. Generally, the states further apart from the Fermi energy are more affected by the change in the moment size. Thus, in comparison with the transverse thermoelectric conductivity, the theoretical estimate for the Hall conductivity is expected to have the larger deviation from experiment. This is because according to Eqs. (3) & (4), the Hall effect is the sum of Berry curva-

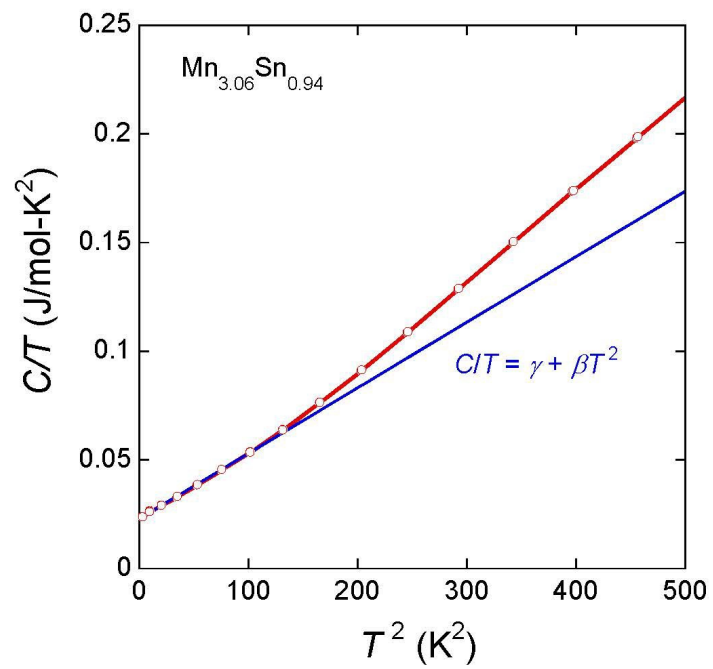
ture of all occupied bands, while the transverse thermoelectric conductivity only derives from the low energy states around E_F . In fact, we found that the disagreement between the theoretical and experimental values of the Hall conductivity is larger than the one for the transverse thermoelectric conductivity (Fig. 3 in the main text).



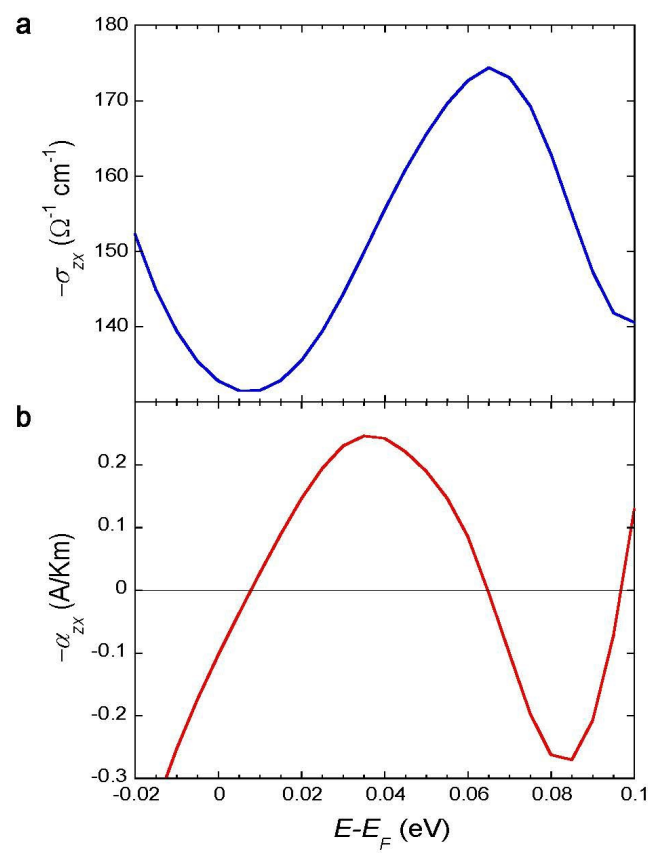
Supplementary Figure S1



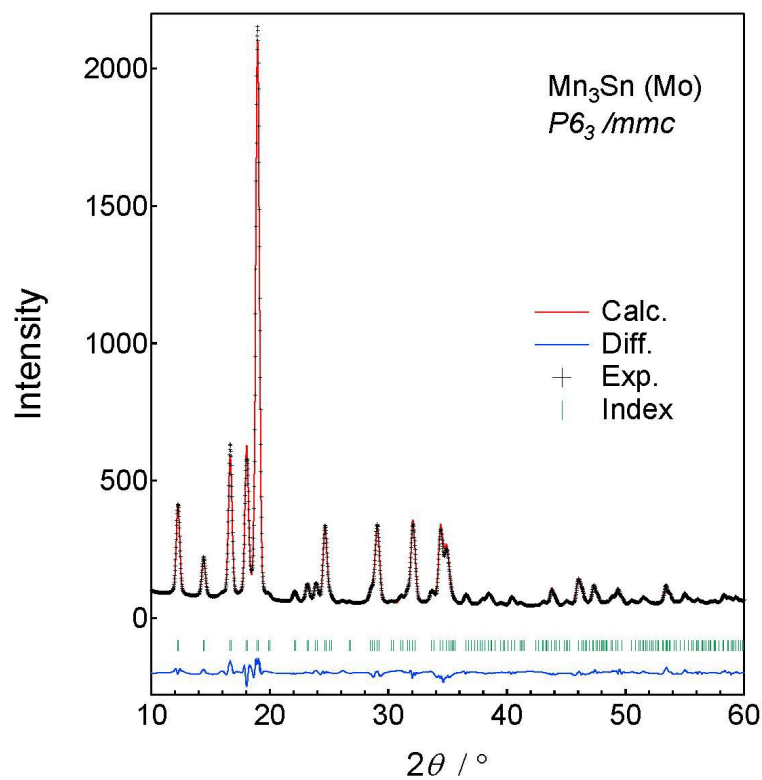
Supplementary Figure S2



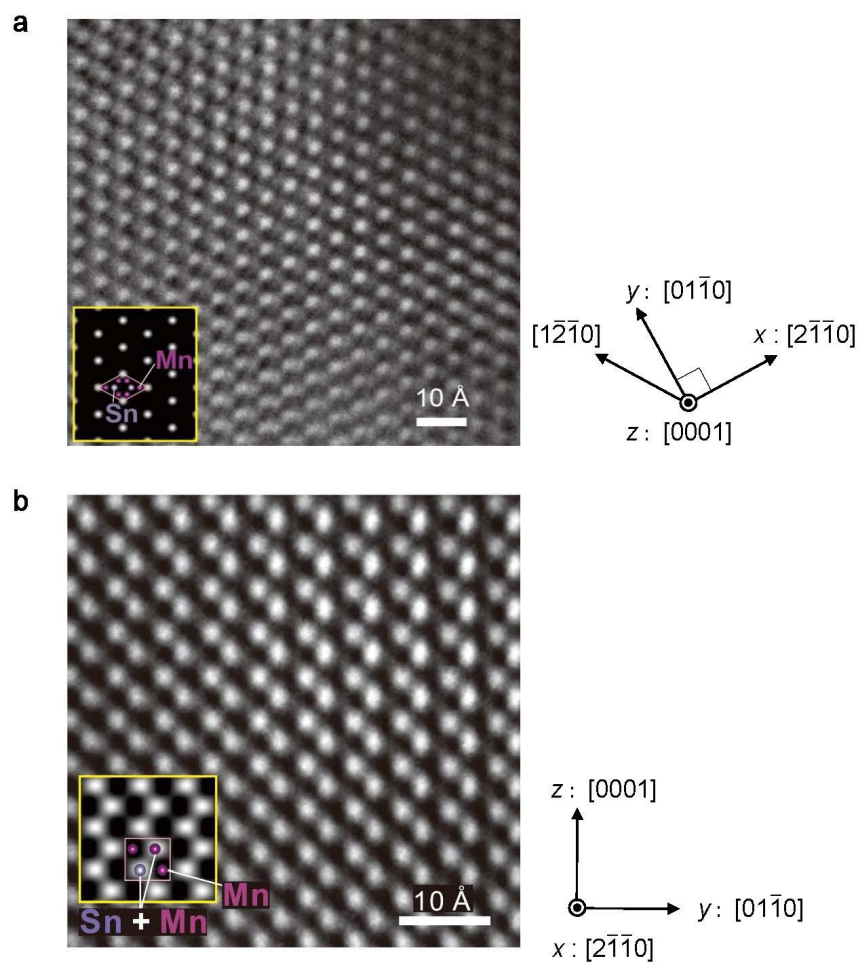
Supplementary Figure S3



Supplementary Figure S4



Supplementary Figure S5



Supplementary Figure S6

Supplementary Figure S1. Temperature dependences of the longitudinal resistivity in Mn₃Sn

Temperature dependence of the longitudinal resistivity $\rho_{ii}(T)$ ($i = x$ (red), y (blue), and z (green)) of **a**, Sample 1 (Mn_{3.06}Sn_{0.94}) and **b**, Sample 2 (Mn_{3.09}Sn_{0.91}) measured at zero field.

Supplementary Figure S2. Magnetic field dependences of the Seebeck coefficient and Nernst effect in Mn₃Sn

a, Field dependence of the Seebeck coefficient S_{ii} ($i = x, y$) at 100 K and 300 K for Sample 1 (Mn_{3.06}Sn_{0.94}). **b**, Field dependence of the Seebeck coefficient S_{ii} ($i = x, y$) at 100 K and 300 K for Sample 2 (Mn_{3.09}Sn_{0.91}). **c**, Field dependence of the Nernst effect $-S_{zx}$ of Sample 1 (Mn_{3.06}Sn_{0.94}) at 350 K, 300 K, 200 K, and 50 K. **d**, Field dependence of the Nernst effect $-S_{zx}$ of Sample 2 (Mn_{3.09}Sn_{0.91}) at 300 K and 200 K. The error-bars are shown if they are larger than the symbol sizes and indicate the measurement errors that come from the uncertainties of their geometrical factors (Methods)

Supplementary Figure S3. Temperature dependence of the specific heat in Mn₃Sn

Specific heat of Sample 1 (Mn_{3.06}Sn_{0.94}) single crystal measured in zero magnetic field divided by temperature C/T (red circle), plotted vs. T^2 . The blue solid line indicates a linear fit at the low temperature region, $2 \leq T \leq 4.5$ K, to estimate γ and β in the Einstein-Debye equation $C/T = \gamma + \beta T^2$. The fit gives the values $\gamma = 22.7 \pm 0.2$ mJ mol⁻¹ K⁻² and $\beta = 0.300 \pm 0.015$ mJ mol⁻¹ K⁻⁴.

Supplementary Figure S4. Energy dependence of the anomalous Hall conductivity and anomalous transverse thermoelectric conductivity

Energy dependence of **a**, the anomalous Hall conductivity $-\sigma_{zx}$, and **b**, the anomalous trans-

verse thermoelectric conductivity $-\alpha_{zx}$ at $T = 100$ K obtained by the first-principles calculation. E_F stands for the Fermi energy for the stoichiometric Mn_3Sn .

Supplementary Figure S5. X-ray diffraction pattern for Mn_3Sn

Room temperature X-ray diffraction (XRD) patterns of Sample 1 $\text{Mn}_{3.06}\text{Sn}_{0.94}$. The crosses correspond to experimental data and the solid line (red) is for the Rietveld refinement fit. Vertical bars (green) below the curves indicate the peak positions of Mn_3Sn phase. The lower curve (blue) is the difference between the observed and calculated at each step.

Supplementary Figure S6. Transmission electron microscope image

Bright field high resolution lattice image projected from **a**, $[0001]$ and **b**, $[2\bar{1}\bar{1}0]$ directions, compared with simulation image.

Table 1: Crystal structure parameters refined by Rietveld analysis for $\text{Mn}_{3+0.06}\text{Sn}_{1-0.06}$ (Sample 1) with $P6_3/mmc$ structure at 300 K. The lattice parameters and the atomic positions of the Mn site are determined by the analysis, which is made using the X-ray diffraction spectra with $\text{MoK}\alpha$ radiation ($\lambda = 0.7103 \text{ \AA}$). The final R indicators are $R_{\text{WP}}=5.29$, $R_e=9.45$, and $S=0.560$ ⁴³.

$\text{Mn}_{3+0.06}\text{Sn}_{1-0.06}$		$V = 125.747(8) \text{ \AA}^3$			
parameters (\AA)		$a = 5.6624(2)$	$b = 5.6624(2)$	$c = 4.5286(2)$	
Atom	Wyckoff position	x	y	z	Occupancy
Mn	6h	0.8388(2)	0.6777(3)	1/4	1
Sn/Mn	2c	1/3	2/3	1/4	(0.94/0.06)

Table 2: Crystal structure parameters refined by Rietveld analysis for $\text{Mn}_{3+0.09}\text{Sn}_{1-0.09}$ (Sample 2) with $P6_3/mmc$ structure at 300 K. The lattice parameters and the atomic positions of the Mn site are determined by the analysis, which is made using the X-ray diffraction spectra with $\text{MoK}\alpha$ radiation ($\lambda = 0.7103 \text{ \AA}$). The final R indicators are $R_{\text{WP}}= 4.35$, $R_e=13.0$, and $S=0.334$ ⁴³.

$\text{Mn}_{3+0.09}\text{Sn}_{1-0.09}$		$125.623(9) \text{ \AA}^3$			
parameters (\AA)		$a = 5.6587(2)$	$b = 5.6587(2)$	$c = 4.5300(2)$	
Atom	Wyckoff position	x	y	z	Occupancy
Mn	6h	0.8402(2)	0.6803(3)	1/4	1
Sn/Mn	2c	1/3	2/3	1/4	(0.91/0.09)